Supplementary information

Modeling NK-cell lymphoma in mice reveals its cell-of-origin and microenvironmental changes and identifies therapeutic targets

Junji Koya[1,2,20], Tomohiko Tanigawa[1,2,20], Kota Mizuno[1,2], Haryoon Kim[1,2], Yuta Ito[1,3], Mitsuhiro Yuasa[1,4], Kentaro Yamaguchi[1,2], Yasunori Kogure[1], Yuki Saito[1,5], Sumito Shingaki[1], Mariko Tabata[1,6], Koichi Murakami[1,2], Kenichi Chiba[7], Ai Okada[7], Yuichi Shiraishi[7], Amira Marouf[8], Raphaël Liévin[8], Sammara Chaubard[9], Arnaud Jaccard[9], Olivier Hermine[8,10], Laurence de Leval[11], Olivier Tournilhac[12], Gandhi Damaj[13], Philippe Gaulard[14,15], Lucile Couronné[8,16], Teruhito Yasui[17,18], Kazutaka Nakashima[19], Hiroaki Miyoshi[19], Koichi Ohshima[19], and Keisuke Kataoka[1,2]*

1. Division of Molecular Oncology, National Cancer Center Research Institute, Tokyo, Japan.
2. Division of Hematology, Department of Medicine, Keio University School of Medicine, Tokyo, Japan.
3. Division of Clinical Oncology and Hematology, Department of Internal Medicine, The Jikei University School of Medicine, Tokyo, Japan.
4. Department of Pathology, Graduate School of Medicine, The University of Tokyo, Tokyo, Japan.
5. Department of Gastroenterology, Keio University School of Medicine, Tokyo, Japan.
6. Department of Urology, Graduate School of Medicine, The University of Tokyo, Tokyo, Japan.
7. Division of Genome Analysis Platform Development, National Cancer Center Research Institute, Tokyo, Japan.

8. Laboratory of cellular and molecular mechanisms of hematological disorders and therapeutic implications, INSERM UMR_S 1163, Imagine Institute, Université Paris Cité, Paris, France.
9. Hematology department, Limoges University Hospital, Limoges, France.
10. Hematology Department, Necker Children's Hospital, Assistance Publique - Hôpitaux de Paris (APHP), Paris, France.
11. Institute of Pathology, Department of Laboratory Medicine and Pathology, Lausanne University Hospital and Lausanne University, Lausanne, Switzerland.
12. Department of Hematology, Clermont-Ferrand University Hospital, Clermont Auvergne University, Clermont-Ferrand, France.
13. Department of Hematology, Caen University Hospital, Normandy University, Caen, France.
14. University Paris Est Créteil, INSERMU955, IMRB, Créteil, France.
15. Pathology Department, Henri Mondor University Hospital, Assistance Publique - Hôpitaux de Paris (APHP), Créteil, France.
16. Laboratory of Onco-Hematology, Necker Children's Hospital, Assistance Publique - Hôpitaux de Paris (APHP), Paris, France.
17. Laboratory of Infectious Diseases and Immunity, Microbial Research Center for Health and Medicine, National Institutes of Biomedical Innovation, Health, and Nutrition, Ibaraki city, Japan.
18. Division of Molecular Psychoneuroimmunology, Institute for Genetic Medicine, Hokkaido University, Sapporo, Japan
19. Division of Pathology, Kurume University, Fukuoka, Japan.
20. These authors contributed equally as co-first authors: Junji Koya and Tomohiko Tanigawa

*Corresponding authors: Keisuke Kataoka (kkataoka-tky@umin.ac.jp)

Supplementary Figures and legends

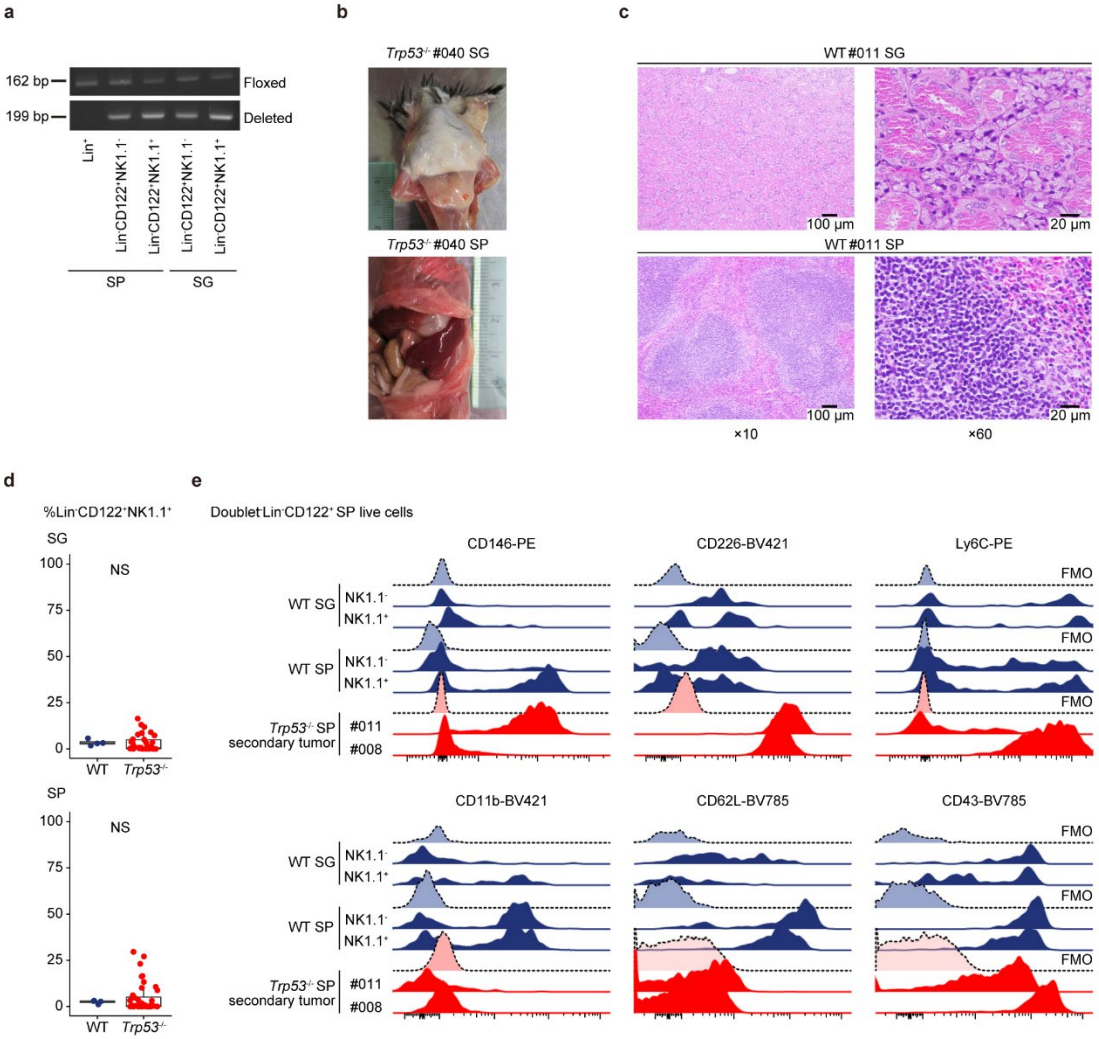

Supplementary Fig. 1. *Trp53* disruption induces NK-cell lymphomas after long latency.

a, PCR detection of the *Trp53* deletion in Lin (Gr1, Ter119, CD19, and CD3)$^+$ cells as well as Lin$^-$CD122$^+$NK1.1$^-$ and Lin$^-$CD122$^+$NK1.1$^+$ NK cells in SP and SG.

b, Representative images of gross appearance of *Trp53*$^{-/-}$ tumors in SG and SP.

c, Representative image of hematoxylin and eosin staining of SG and SP from WT (at 8 weeks old) mice.

d, Proportion of Lin$^-$CD122$^+$NK1.1$^+$ cells in SG and SP from WT (n = 4 at 60 weeks old) and *Trp53*$^{-/-}$ (n = 40 at tumor onset) mice. Box plots show medians (lines), IQRs (boxes), and ± 1.5 × IQR (whiskers). NS: not significant, two-sided Welch's t-test. Source data are provided as a Source Data file.

e, Representative histograms of CD146, CD226, Ly6C, CD11b, CD62L and CD43 expression in $Lin^{-}CD122^{+}NK1.1^{-}$ and $Lin^{-}CD122^{+}NK1.1^{+}$ cells in SG and SP from WT mice (at 8 weeks old) and *Trp53*$^{-/-}$ secondary tumors in SP. Fluorescence minus one (FMO) controls are shown as shaded histograms.

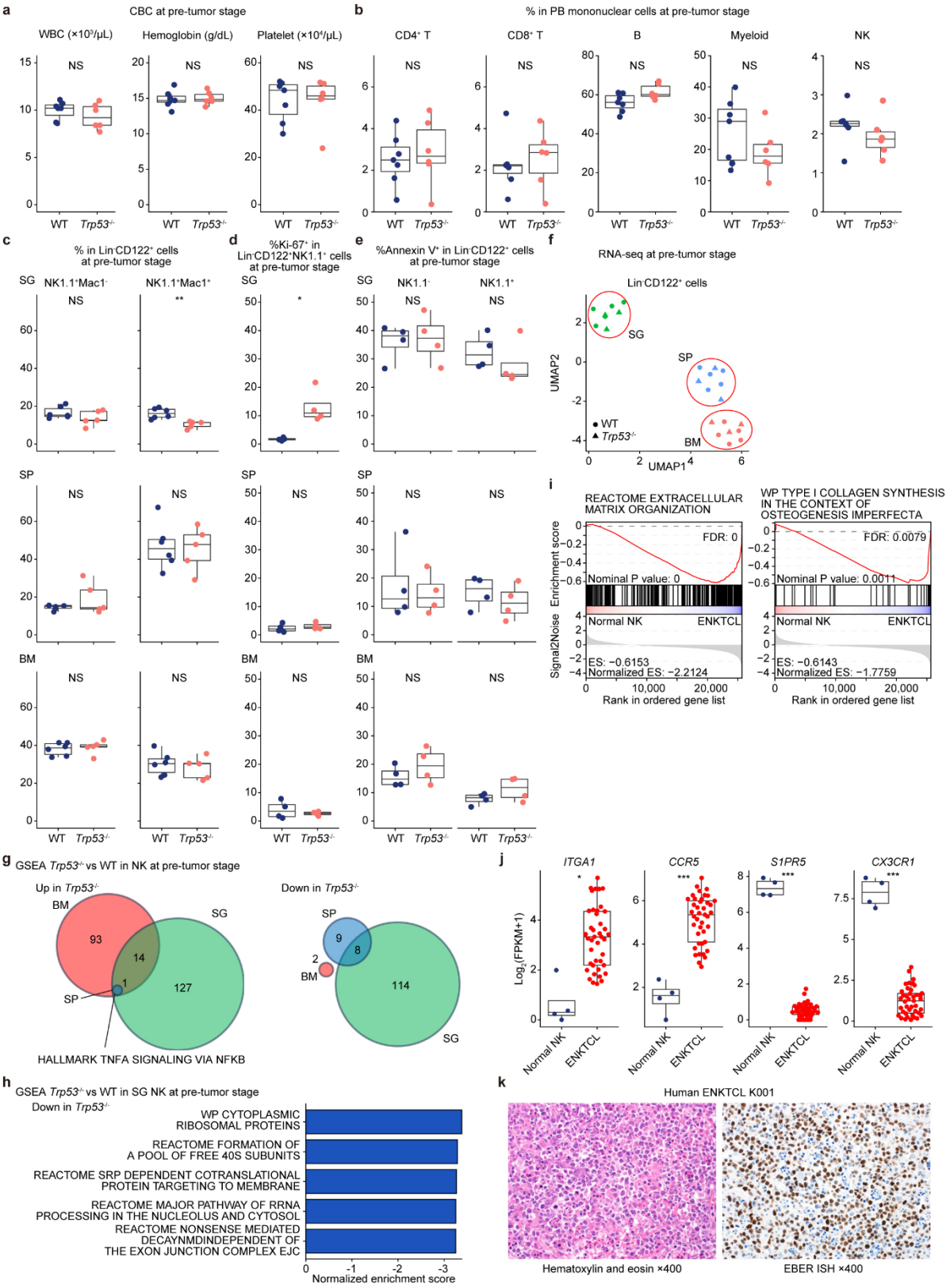
a
CBC at pre-tumor stage
WBC (×10³/μL)
Hemoglobin (g/dL)
Platelet (×10⁴/μL)
b
% in PB mononuclear cells at pre-tumor stage
CD4⁺ T
CD8⁺ T
B
Myeloid
NK
NS
WT
Trp53-/-
c
% in Lin⁻CD122⁺ cells at pre-tumor stage
SG
SP
BM
NK1.1⁺Mac1⁻
NK1.1⁺Mac1⁺
d
%Ki-67⁺ in Lin⁻CD122⁺NK1.1⁺ cells at pre-tumor stage
e
%Annexin V⁺ in Lin⁻CD122⁺ cells at pre-tumor stage
NK1.1⁻
NK1.1⁺
f
RNA-seq at pre-tumor stage
Lin⁻CD122⁺ cells
UMAP1
UMAP2
i
REACTOME EXTRACELLULAR MATRIX ORGANIZATION
FDR: 0
Nominal P value: 0
WP TYPE I COLLAGEN SYNTHESIS IN THE CONTEXT OF OSTEOGENESIS IMPERFECTA
FDR: 0.0079
Nominal P value: 0.0011
Enrichment score
Signal2Noise
Normal NK
ENKTCL
ES: −0.6153
Normalized ES: −2.2124
ES: −0.6143
Normalized ES: −1.7759
Rank in ordered gene list
g
GSEA Trp53-/- vs WT in NK at pre-tumor stage
Up in Trp53-/-
Down in Trp53-/-
93
14
1
127
9
8
2
114
HALLMARK TNFA SIGNALING VIA NFKB
h
GSEA Trp53-/- vs WT in SG NK at pre-tumor stage
Down in Trp53-/-
WP CYTOPLASMIC RIBOSOMAL PROTEINS
REACTOME FORMATION OF A POOL OF FREE 40S SUBUNITS
REACTOME SRP DEPENDENT COTRANSLATIONAL PROTEIN TARGETING TO MEMBRANE
REACTOME MAJOR PATHWAY OF RRNA PROCESSING IN THE NUCLEOLUS AND CYTOSOL
REACTOME NONSENSE MEDIATED DECAYNMDINDEPENDENT OF THE EXON JUNCTION COMPLEX EJC
Normalized enrichment score
j
ITGA1
CCR5
S1PR5
CX3CR1
Log2(FPKM+1)
k
Human ENKTCL K001
Hematoxylin and eosin ×400
EBER ISH ×400

70

71

Supplementary Fig. 2. Differential phenotypes of *Trp53*$^{-/-}$ NK cells at the pre-tumor stage across tissues.

a, CBC in PB of WT (n = 7) and *Trp53*$^{-/-}$ (n = 6) mice (at 8 weeks old).

b, Proportion of CD4^{+} T, CD8^{+} T, B, myeloid, and NK cells in PB from WT (n = 7) and *Trp53*$^{-/-}$ (n = 6) mice (at 8 weeks old).

c, Proportion of NK1.1^{+}Mac1^{-} and NK1.1^{+}Mac1^{+} cells in Lin^{-}CD122^{+} cells in SG, SP, and BM from WT (n = 6) and *Trp53*$^{-/-}$ (n = 5) mice (at 8 weeks old).

d, Proportion of Ki-67^{+} cells in Lin^{-}CD122^{+}NK1.1^{+} cells in SG, SP, and BM from WT (n = 4) and *Trp53*$^{-/-}$ (n = 4) mice (at 8 weeks old).

e, Proportion of Annexin V^{+} cells in Lin^{-}CD122^{+}NK1.1^{-} and Lin^{-}CD122^{+}NK1.1^{+} cells in SG, SP, and BM from WT (n = 4) and *Trp53*$^{-/-}$ (n = 4) mice at the pre-tumor stage (at 8 weeks).

f, UMAP (uniform manifold approximation and projection) plot of RNA-seq expression data of sorted Lin^{-}CD122^{+} NK cells in SG, SP, and BM from WT (circle, n = 5) and *Trp53*$^{-/-}$ (triangle, n = 3) mice (at 8 weeks old).

g, GSEA analysis of expression data comparing WT (n = 5 each for SG, SP, and BM) and *Trp53*$^{-/-}$ (n = 3 each for SG, SP, and BM) Lin^{-}CD122^{+} NK cells across SG, SP, and BM (at 8 weeks old). Venn diagrams depict the overlap of upregulated (left) and downregulated signatures (right). Signatures with FDR < 0.25 are considered significant.

h, The top five downregulated signatures in GSEA analysis of expression data comparing WT (n = 5) and *Trp53*$^{-/-}$ (n = 3) Lin^{-}CD122^{+} NK cells in SG (at 8 weeks old).

i, Significant enrichment of extracellular matrix-associated signatures in GSEA analysis of expression data comparing human normal NK cells (n = 4) and ENKTCL tumors (n = 41).

j, Expression of genes associated with tissue-resident (*ITGA1* and *CCR5*) and circulating (*S1PR5* and *CX3CR1*) NK cells in human normal NK cells (n = 4) and ENKTCL tumors (n = 41) by RNA-seq.

k, Representative image of hematoxylin and eosin staining (left) and EBV-encoded small RNA (EBER) in situ hybridization (right) in a human ENKTCL sample.

a-e, and j, Box plots show medians (lines), IQRs (boxes), and ± 1.5 × IQR (whiskers). NS: not significant, *P < 0.05, **P < 0.005, ***P < 0.0005, two-sided Welch's t-test. Source data are provided as a Source Data file.

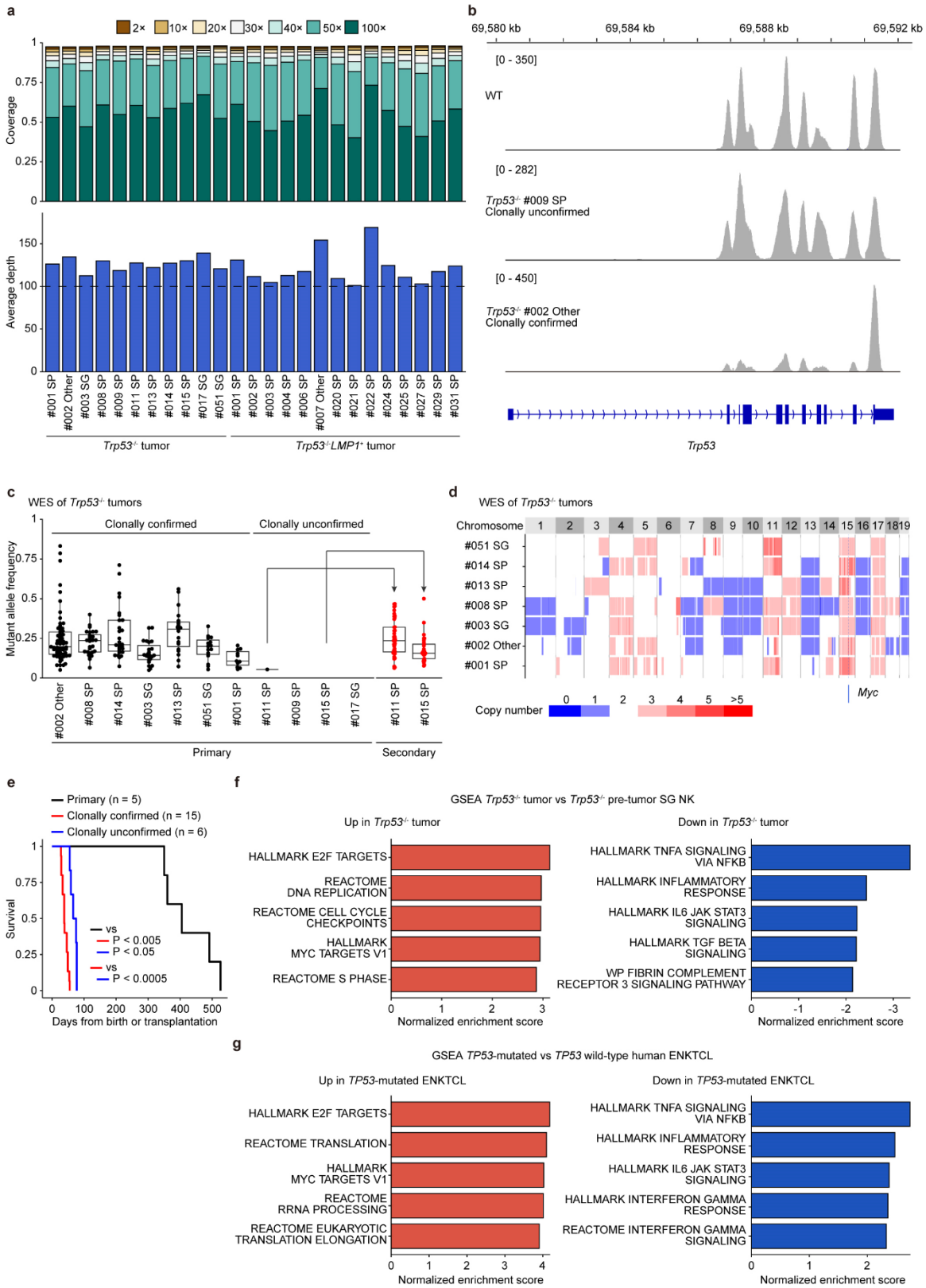
a
2× 10× 20× 30× 40× 50× 100×
Coverage
Average depth
#001 SP
#002 Other
#003 SG
#008 SP
#009 SP
#011 SP
#013 SP
#014 SP
#015 SP
#017 SG
#051 SG
#001 SP
#002 SP
#003 SP
#004 SP
#006 SP
#007 Other
#020 SP
#021 SP
#022 SP
#024 SP
#025 SP
#027 SP
#029 SP
#031 SP
Trp53-/- tumor
Trp53-/-LMP1+ tumor
b
69,580 kb
69,584 kb
69,588 kb
69,592 kb
[0 - 350]
WT
[0 - 282]
Trp53-/- #009 SP
Clonally unconfirmed
[0 - 450]
Trp53-/- #002 Other
Clonally confirmed
Trp53
c
WES of Trp53-/- tumors
Clonally confirmed
Clonally unconfirmed
Mutant allele frequency
#002 Other
#008 SP
#014 SP
#003 SG
#013 SP
#051 SG
#001 SP
#011 SP
#009 SP
#015 SP
#017 SG
#011 SP
#015 SP
Primary
Secondary
d
WES of Trp53-/- tumors
Chromosome
#051 SG
#014 SP
#013 SP
#008 SP
#003 SG
#002 Other
#001 SP
Myc
Copy number
e
Primary (n = 5)
Clonally confirmed (n = 15)
Clonally unconfirmed (n = 6)
Survival
vs
P < 0.005
P < 0.05
vs
P < 0.0005
Days from birth or transplantation
f
GSEA Trp53-/- tumor vs Trp53-/- pre-tumor SG NK
Up in Trp53-/- tumor
HALLMARK E2F TARGETS
REACTOME DNA REPLICATION
REACTOME CELL CYCLE CHECKPOINTS
HALLMARK MYC TARGETS V1
REACTOME S PHASE
Normalized enrichment score
Down in Trp53-/- tumor
HALLMARK TNFA SIGNALING VIA NFKB
HALLMARK INFLAMMATORY RESPONSE
HALLMARK IL6 JAK STAT3 SIGNALING
HALLMARK TGF BETA SIGNALING
WP FIBRIN COMPLEMENT RECEPTOR 3 SIGNALING PATHWAY
Normalized enrichment score
g
GSEA TP53-mutated vs TP53 wild-type human ENKTCL
Up in TP53-mutated ENKTCL
HALLMARK E2F TARGETS
REACTOME TRANSLATION
HALLMARK MYC TARGETS V1
REACTOME RRNA PROCESSING
REACTOME EUKARYOTIC TRANSLATION ELONGATION
Normalized enrichment score
Down in TP53-mutated ENKTCL
HALLMARK TNFA SIGNALING VIA NFKB
HALLMARK INFLAMMATORY RESPONSE
HALLMARK IL6 JAK STAT3 SIGNALING
HALLMARK INTERFERON GAMMA RESPONSE
REACTOME INTERFERON GAMMA SIGNALING
Normalized enrichment score

Supplementary Fig. 3. Genomic and transcriptomic characterization of NK-cell tumors.

a, The percentage of targeted bases covered by at least 2×, 10×, 20×, 30×, 40×, 50×, and 100× sequencing reads (top) and average read depth (bottom) are shown for a total of 25 WES samples.

b, Detection of *Trp53* deletion targeting exons 3–11 in clonally confirmed *Trp53*$^{-/-}$ tumors. WES read depths are visualized by IGV.

c, Hierarchy of somatic mutations with allele frequencies in *Trp53*$^{-/-}$ tumors (n = 13) detected by WES. Clonality is considered confirmed if > 3 somatic mutations are detected. 11 primary tumors and 2 secondary tumors transplanted from clonally unconfirmed tumors are shown. Box plots show medians (lines), IQRs (boxes), and ± 1.5 × IQR (whiskers).

d, Heatmap showing somatic CNA segments in each sample (vertical axis) plotted by chromosomal location (horizontal vertical axis) in *Trp53*$^{-/-}$ clonally confirmed tumors (n = 7).

e, Kaplan-Meier survival curves of secondary mice (n = 21) transplanted with 1×10^6 clonally confirmed (n = 15) and unconfirmed (n = 6) *Trp53*$^{-/-}$ tumor cells compared with the corresponding primary mice. (n = 5). Data are the same as in **Fig. 1h**. Log-rank test.

f, GSEA analysis of expression data comparing *Trp53*$^{-/-}$ tumors (n = 4) and *Trp53*$^{-/-}$ Lin$^-$CD122$^+$ NK cells in SG (n = 3 at 8 weeks old).

g, GSEA analysis of expression data comparing human *TP53* WT (n = 18) and *TP53*-mutated (n = 2) ENKTCL tumors.

f, g, Top five upregulated and downregulated signatures are shown. Signatures with FDR < 0.25 are considered significant.

c, e, Source data are provided as a Source Data file.

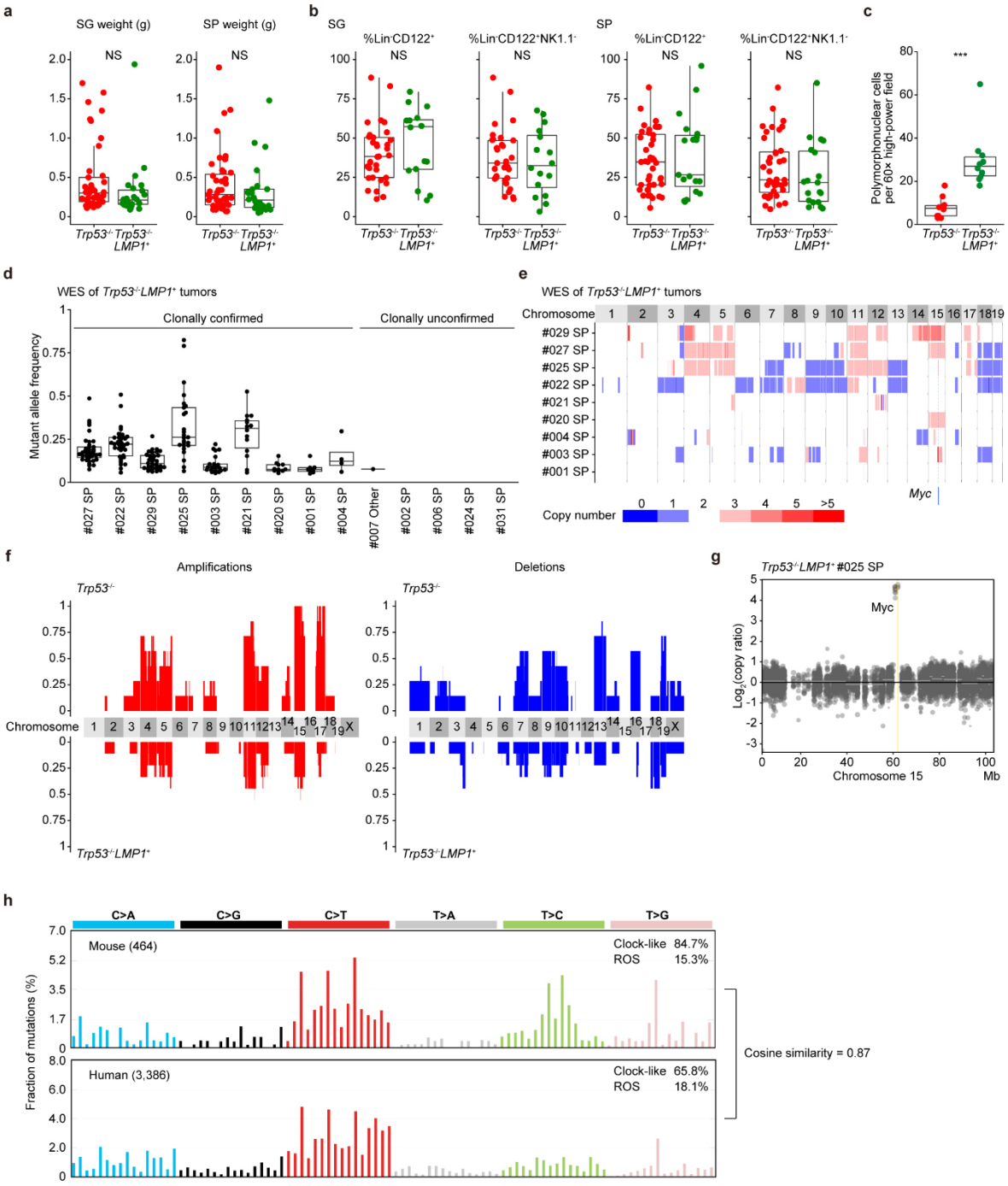
a
SG weight (g)
SP weight (g)
NS
b
SG
SP
%Lin-CD122+
%Lin-CD122+NK1.1-
c
***
Polymorphonuclear cells per 60x high-power field
Trp53-/- Trp53-/- LMP1+
d
WES of Trp53-/-LMP1+ tumors
Clonally confirmed
Clonally unconfirmed
Mutant allele frequency
#027 SP
#022 SP
#029 SP
#025 SP
#003 SP
#021 SP
#020 SP
#001 SP
#004 SP
#007 Other
#002 SP
#006 SP
#024 SP
#031 SP
e
Chromosome
#029 SP
#027 SP
#025 SP
#022 SP
#021 SP
#020 SP
#004 SP
#003 SP
#001 SP
Myc
Copy number
f
Amplifications
Deletions
Trp53-/-
Trp53-/-LMP1+
g
Trp53-/-LMP1+ #025 SP
Myc
Log2(copy ratio)
Chromosome 15
Mb
h
C>A
C>G
C>T
T>A
T>C
T>G
Mouse (464)
Clock-like 84.7%
ROS 15.3%
Human (3,386)
Clock-like 65.8%
ROS 18.1%
Fraction of mutations (%)
Cosine similarity = 0.87

128

129

Supplementary Fig. 4. Phenotypic and genetic characteristics of *Trp53*$^{-/-}$*LMP1*$^{+}$ tumors.

a, SG and SP weights of *Trp53*$^{-/-}$ (n = 41) and *Trp53*$^{-/-}$*LMP1*$^{+}$ (n = 24) mice (at tumor onset). *Trp53*$^{-/-}$ data are the same as in **Fig. 1c**.

b, Proportion of Lin^{-}, Lin^{-}CD122^{+}, and Lin^{-}CD122^{+}NK1.1^{-} cells in SG and SP from *Trp53*$^{-/-}$ (n = 40) and *Trp53*$^{-/-}$*LMP1*$^{+}$ (n = 19) mice (at tumor onset). *Trp53*$^{-/-}$ data are the same as in **Fig. 1g**.

c, Number of polymorphonuclear cells per 60× high-power field in hematoxylin and eosin-stained sections of *Trp53*$^{-/-}$ and *Trp53*$^{-/-}$*LMP1*$^{+}$ tumors in SP. Five randomly chosen fields from each of two mice were examined per genotype.

d, Hierarchy of somatic mutations with allele frequencies in *Trp53*$^{-/-}$*LMP1*$^{+}$ tumors (n = 14) detected by WES.

e, Heatmap showing somatic CNA segments in each sample (vertical axis) plotted by chromosomal location (horizontal axis) in *Trp53*$^{-/-}$*LMP1*$^{+}$ clonally confirmed tumors (n = 9).

f, Frequencies of copy number amplifications and deletions across the genome in *Trp53*$^{-/-}$ (n = 7) and *Trp53*$^{-/-}$*LMP1*$^{+}$ clonally confirmed tumors (n = 9).

g, *Myc* amplification in a representative *Trp53*$^{-/-}$*LMP1*$^{+}$ tumor (#025 SP)

h, De novo mutational signatures extracted from 464 mutations in 25 mouse NK-cell tumors (11 *Trp53*$^{-/-}$ and 14 *Trp53*$^{-/-}$*LMP1*$^{+}$ tumors) and 3,386 mutations in 66 human ENKTCL samples[1] detected by WES. Known related etiologies are noted. Cosine similarities between mouse and human de novo signatures are shown.

a-d, Box plots show medians (lines), IQRs (boxes), and ± 1.5 × IQR (whiskers). NS: not significant, ***P < 0.0005, two-sided Welch's t-test. Source data are provided as a Source Data file.

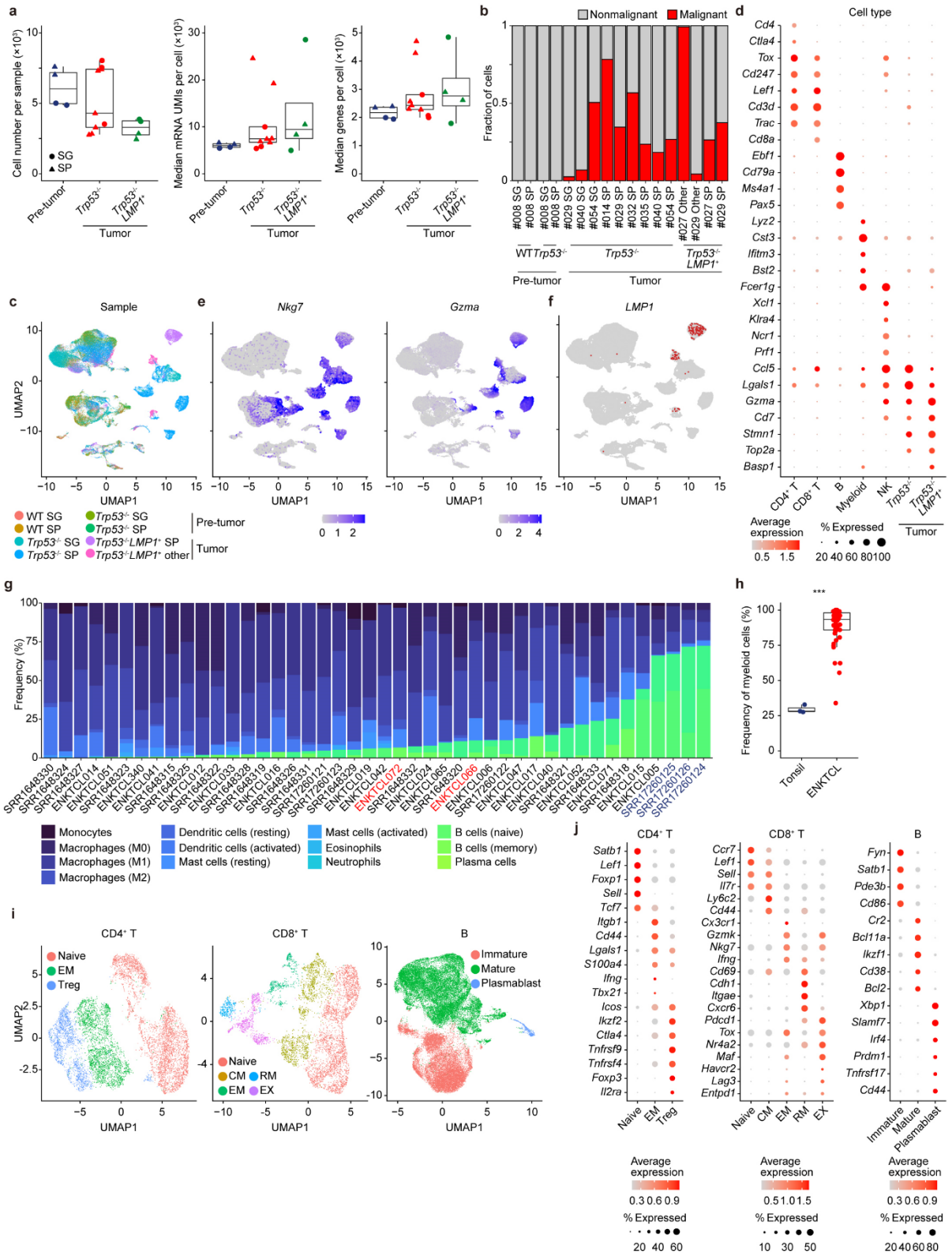

Supplementary Fig. 5. scRNA-seq analysis of *Trp53*$^{-/-}$ and *Trp53*$^{-/-}$*LMP1*$^{+}$ tumors.

a, Quality control of datasets regarding analyzed cell number, median mRNA unique molecular identifier (UMI) counts per cell, and median detected genes for each sample.

b, The fraction of malignant cells in each sample.

c, UMAP plot (same as **Fig. 4a**) colored by sample.

d, Bubble plot of representative mRNA markers for each cluster.

e, Normalized mRNA levels of *Nkg7* and *Gzma* on UMAP plots in **Fig. 4a**.

f, Distribution of *LMP1*-expressing cells on UMAP plot in **Fig. 4a**.

g, CIBERSORTx deconvolution of RNA-seq data of 41 human ENKTCL tumors and 3 normal tonsils. Proportion in nonmalignant cells (after excluding T and NK cells) are shown. Normal tonsils and *TP53*-mutated tumors are colored in blue and red, respectively.

h, Proportion of myeloid cells (after excluding T and NK cells) in 41 human ENKTCL tumors and 3 normal tonsils. ***P < 0.0005, two-sided Welch's t-test. Source data are provided as a Source Data file.

i, UMAP plot of subclustering of $CD4^+$ T cells (left), $CD8^+$ T cells (middle), and B cells (right).

j, Bubble plot of representative mRNA markers for each $CD4^+$ T-cell (left), $CD8^+$ T-cell (middle), and B-cell (right) subcluster.

a,h, Box plots show medians (lines), IQRs (boxes), and ± 1.5 × IQR (whiskers).

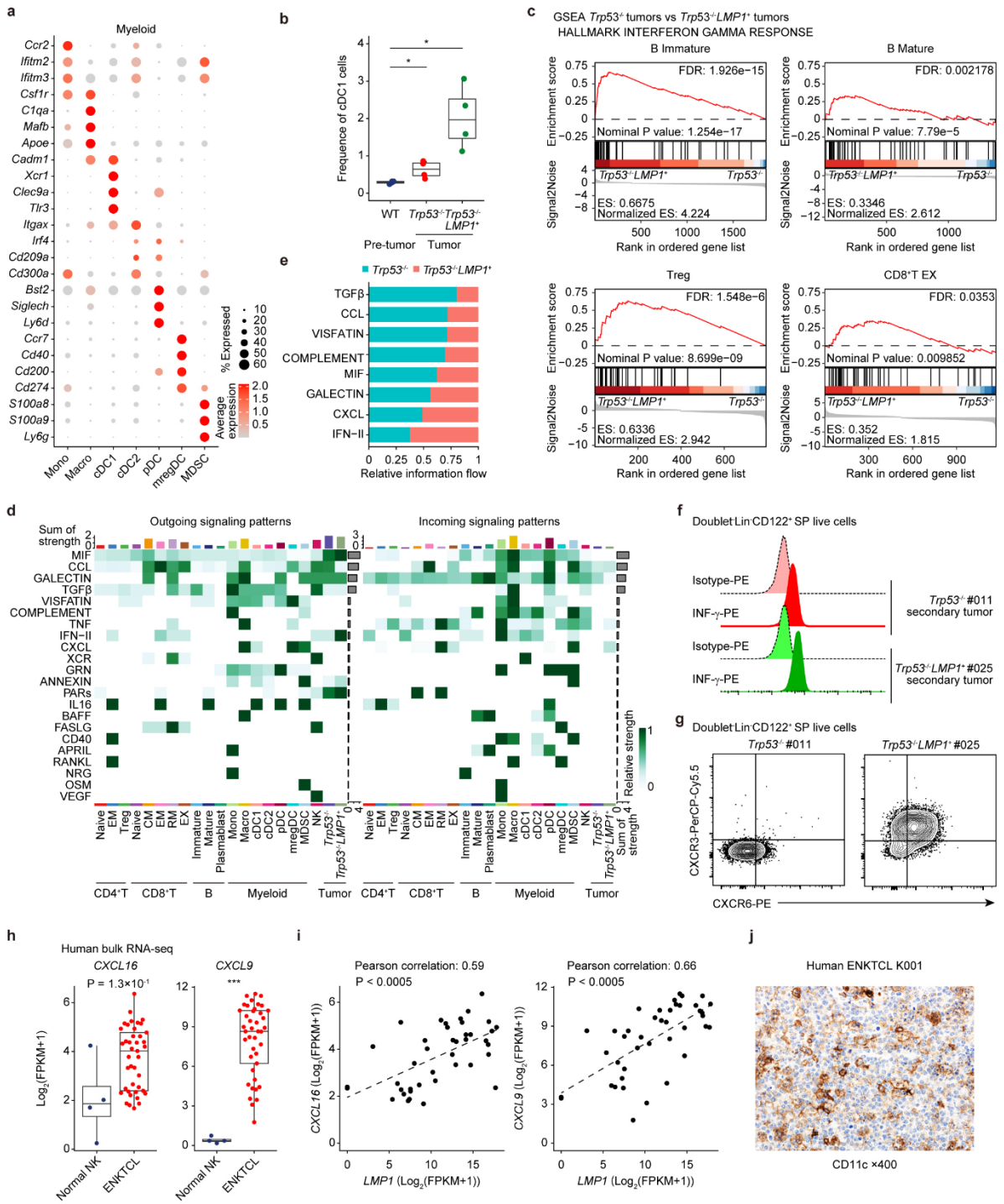
a
Myeloid
Ccr2
Ifitm2
Ifitm3
Csf1r
C1qa
Mafb
Apoe
Cadm1
Xcr1
Clec9a
Tlr3
Itgax
Irf4
Cd209a
Cd300a
Bst2
Siglech
Ly6d
Ccr7
Cd40
Cd200
Cd274
S100a8
S100a9
Ly6g
Mono
Macro
cDC1
cDC2
pDC
mregDC
MDSC
% Expressed
Average expression
b
Frequence of cDC1 cells
WT
Trp53-/-
Trp53-/- LMP1+
Pre-tumor
Tumor
c
GSEA Trp53-/- tumors vs Trp53-/-LMP1+ tumors
HALLMARK INTERFERON GAMMA RESPONSE
B Immature
FDR: 1.926e−15
Nominal P value: 1.254e−17
ES: 0.6675
Normalized ES: 4.224
B Mature
FDR: 0.002178
Nominal P value: 7.79e−5
ES: 0.3346
Normalized ES: 2.612
Treg
FDR: 1.548e−6
Nominal P value: 8.699e−09
ES: 0.6336
Normalized ES: 2.942
CD8+T EX
FDR: 0.0353
Nominal P value: 0.009852
ES: 0.352
Normalized ES: 1.815
Enrichment score
Signal2Noise
Rank in ordered gene list
e
Trp53-/-
Trp53-/-LMP1+
TGFβ
CCL
VISFATIN
COMPLEMENT
MIF
GALECTIN
CXCL
IFN−II
Relative information flow
d
Outgoing signaling patterns
Incoming signaling patterns
Sum of strength
MIF
CCL
GALECTIN
TGFβ
VISFATIN
COMPLEMENT
TNF
IFN−II
CXCL
XCR
GRN
ANNEXIN
PARs
IL16
BAFF
FASLG
CD40
APRIL
RANKL
NRG
OSM
VEGF
Relative strength
Naive
EM
Treg
Naive
CM
EM
RM
EX
Immature
Mature
Plasmablast
Mono
Macro
cDC1
cDC2
pDC
mregDC
MDSC
NK
Trp53-/-
Trp53-/-LMP1+
CD4+T
CD8+T
B
Myeloid
Tumor
f
Doublet-Lin-CD122+ SP live cells
Isotype-PE
INF-γ-PE
Trp53-/- #011
secondary tumor
Trp53-/-LMP1+ #025
secondary tumor
g
Doublet-Lin-CD122+ SP live cells
Trp53-/- #011
Trp53-/-LMP1+ #025
CXCR3-PerCP-Cy5.5
CXCR6-PE
h
Human bulk RNA-seq
CXCL16
P = 1.3×10-1
CXCL9
***
Log2(FPKM+1)
Normal NK
ENKTCL
i
Pearson correlation: 0.59
P < 0.0005
Pearson correlation: 0.66
P < 0.0005
CXCL16 (Log2(FPKM+1))
CXCL9 (Log2(FPKM+1))
LMP1 (Log2(FPKM+1))
j
Human ENKTCL K001
CD11c ×400

174

175

Supplementary Fig. 6. Cell-cell communication networks in of *Trp53*$^{-/-}$ and *Trp53*$^{-/-}$*LMP1*$^{+}$ tumors, Related to Figure 6.

a, Bubble plot of representative mRNA markers for each myeloid cell subcluster.

b, Proportion of cCD1 cells in SP from WT (at 8 weeks old), *Trp53*$^{-/-}$ (at tumor onset), and *Trp53*$^{-/-}$*LMP1*$^{+}$ (at tumor onset) mice (n = 4 each). Proportion in nonmalignant cells are shown for tumor-bearing mice. *P < 0.05, two-sided Welch's t-test.

c, Significant enrichment of IFN-γ signature in GSEA analysis of scRNA-seq data comparing B Immature, B Mature, Treg, and CD8^{+}T EX subclusters between *Trp53*$^{-/-}$*LMP1*$^{+}$ and *Trp53*$^{-/-}$ tumors.

d, Heatmap showing relative strength of 16 pathways contributing to outgoing (left) or incoming (right) signaling of each cell cluster in CellChat analysis.

e, Comparison of information flow of each signaling between *Trp53*$^{-/-}$ and *Trp53*$^{-/-}$*LMP1*$^{+}$ tumors in CellChat analysis. Nine signaling pathways with information flow ≥ 0.03 are shown.

f, Representative histograms of IFN-γ expressions in Lin^{-}CD122^{+} cells from *Trp53*$^{-/-}$ and *Trp53*$^{-/-}$*LMP1*$^{+}$ tumors. Isotype controls are shown as shaded histograms.

g, Representative plots of CXCR6 and CXCR3 expressions in Lin^{-}CD122^{+} cells from *Trp53*$^{-/-}$ and *Trp53*$^{-/-}$*LMP1*$^{+}$ tumors.

h, *CXCL16* and *CXCL9* gene expressions in human normal NK cells (n = 4) and ENKTCL tumors (n = 41) by RNA-seq. Box plots show medians (lines), IQRs (boxes), and ± 1.5 × IQR (whiskers). ***P < 0.0005, two-sided Welch's t-test.

i, Correlation between *LMP1* expression and *CXCL16* (left) and *CXCL9* (right) gene expressions in 41 human ENKTCL samples. Pearson correlation test.

j, Representative image of CD11c immunostaining in a human ENKTCL sample.

b, h, and i, Source data are provided as a Source Data file.

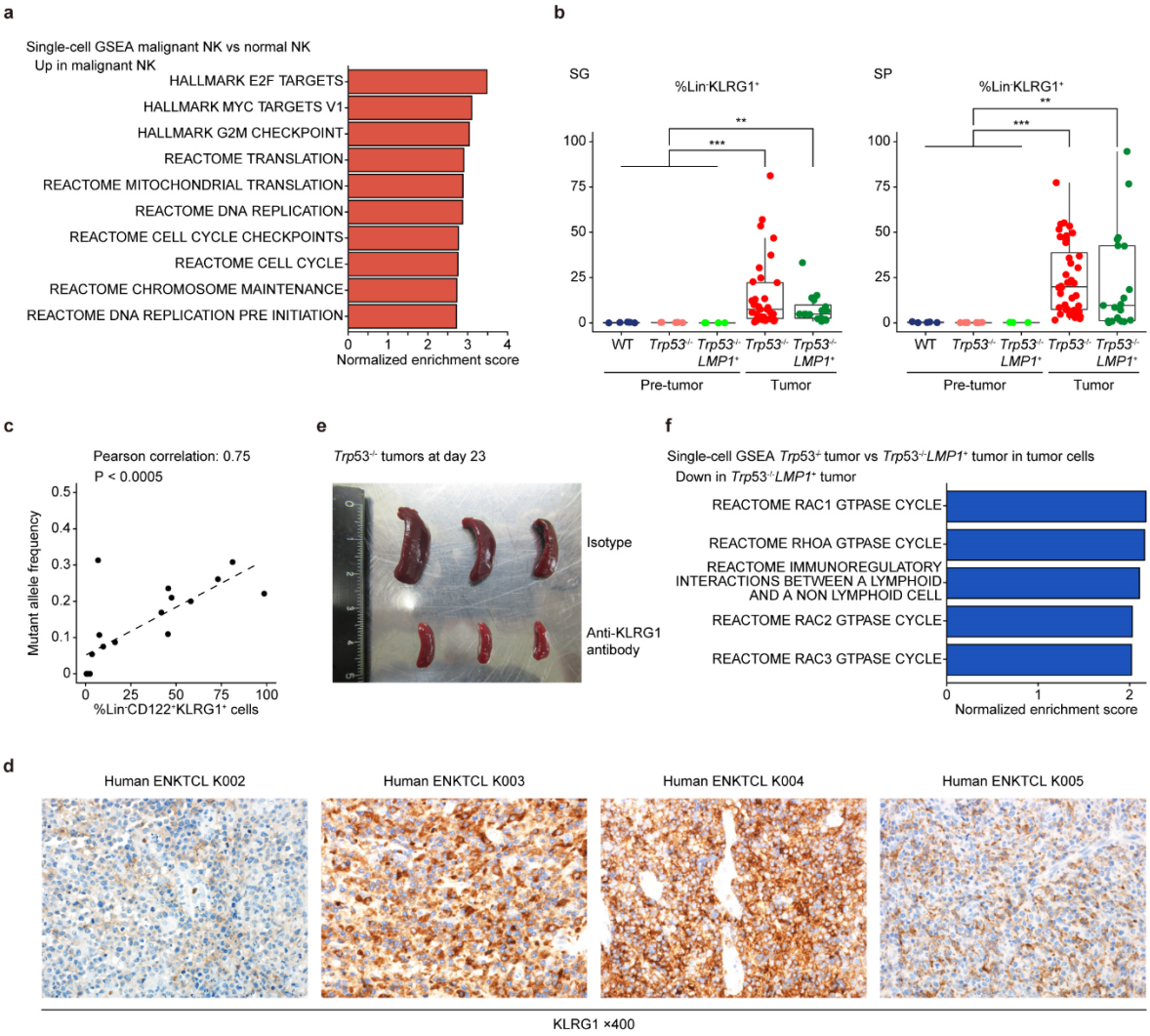

Supplementary Fig. 7. Anti-KLRG1 antibody treatment against murine NK-cell tumors, Related to Figure 7.

a, GSEA analysis of scRNA-seq data comparing normal and malignant (*Trp53*$^{-/-}$ and *Trp53*$^{-/-}$ *LMP1*$^{+}$) NK cells. Top ten upregulated signatures are shown.

b, Proportion of Lin^{-}KLRG1^{+} cells in SG and SP from WT (n = 5 at 8 weeks old), *Trp53*$^{-/-}$ (n = 6 at 8 weeks old and n = 40 at tumor onset), and *Trp53*$^{-/-}$*LMP1*$^{+}$ (n = 4 at 8 weeks old and n = 19 at tumor onset) mice. Box plots show medians (lines), IQRs (boxes), and ± 1.5 × IQR (whiskers). **P < 0.005, ***P < 0.0005, two-sided Welch's t-test.

c, Correlation between the Lin^{-}CD122^{+}KLRG1^{+} fraction and mutant allele frequency in 18 primary tumor samples analyzed by both WES and flow cytometry. Pearson correlation test.

d, Representative images of KLRG1 immunostaining in four additional human ENKTCL samples.

e, SP size (at day 23 post-transplantation) of mice transplanted with 5×10^5 *Trp53*$^{-/-}$ tumor cells and administered with anti-KLRG1 antibody or isotype control.

f, GSEA analysis of scRNA-seq data comparing *Trp53*$^{-/-}$ and *Trp53*$^{-/-}$*LMP1*$^{+}$ malignant NK cells. Top five downregulated signatures in *Trp53*$^{-/-}$*LMP1*$^{+}$ malignant NK cells are shown.

a, f, Signatures with FDR < 0.25 are considered significant.

b, c, Source data are provided as a Source Data file.

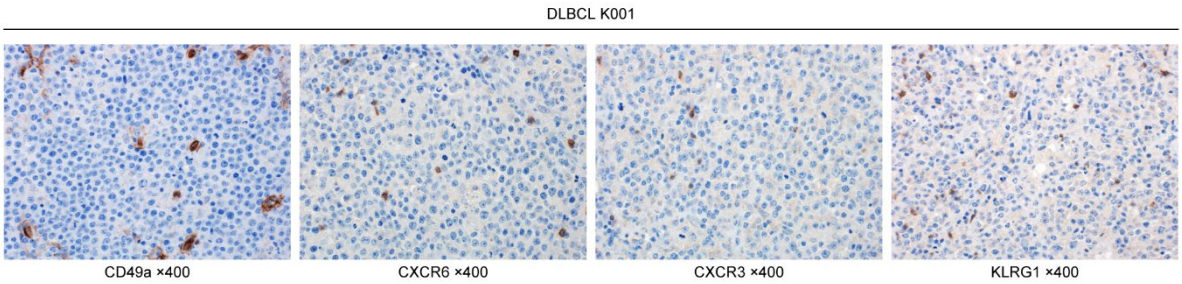

Supplementary Fig. 8. Validation of the specificity of the antibodies used in Immunohistochemical analysis.

Representative images of CD49a, CXCR6, CXCR3, and KLRG1 immunostaining in a human diffuse large B-cell lymphoma (DLBCL) sample.

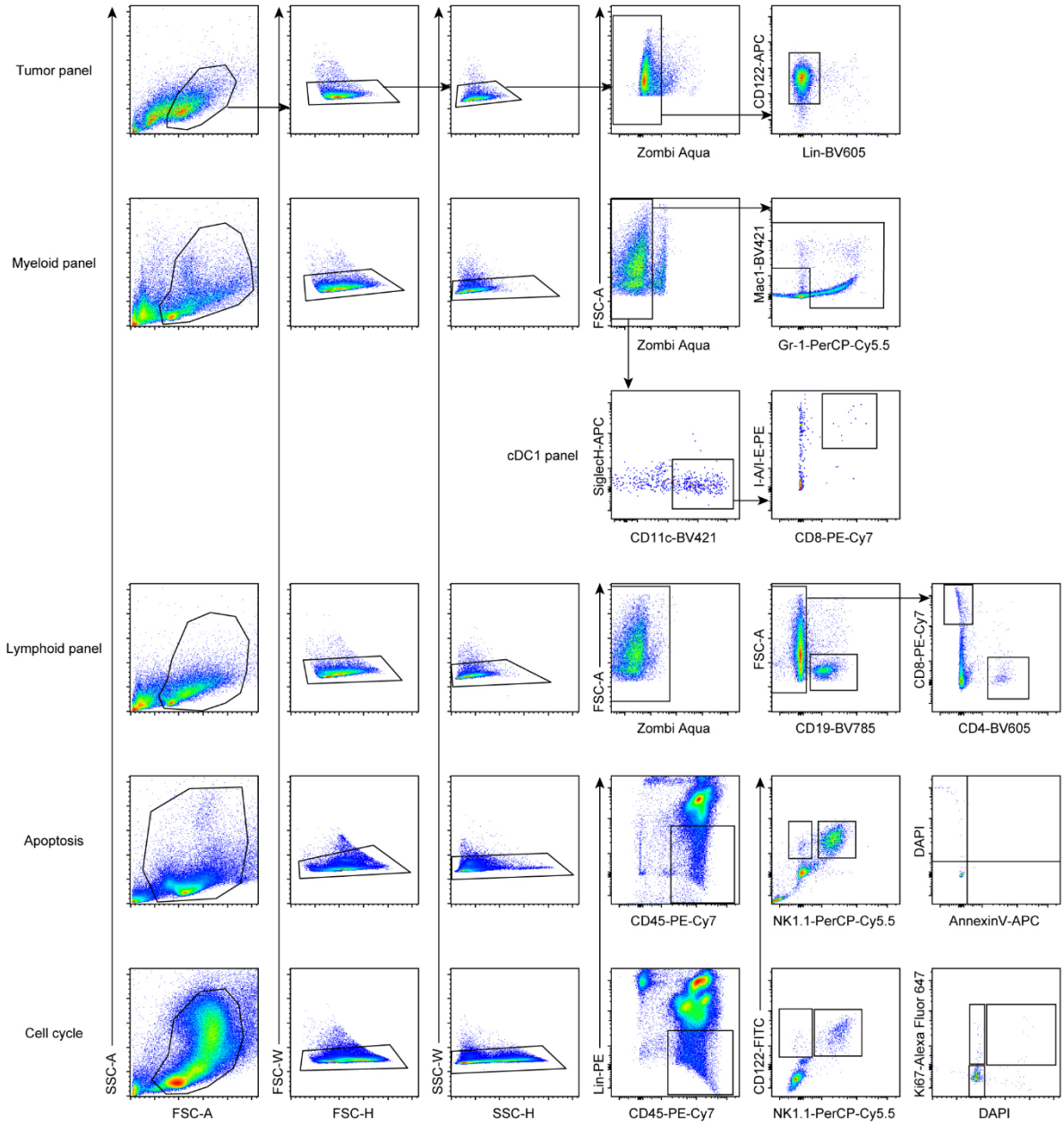

228

229 **Supplementary Fig. 9. Gating strategies of flow cytometric analyses.**

230 Gating strategies of flow cytometric analyses of tumor cells, myeloid cells, lymphoid cells,
231 apoptosis status, and cell cycle status. The tumor panel was used in **Fig. 1e, 1f, 1g, 2a, 2e,**
232 **5e, 5g, 6b, Supplementary Fig. 1d, Supplementary Fig. 1e, Supplementary Fig. 2c,**
233 **Supplementary Fig. 4b, Supplementary Fig. 6f, Supplementary Fig. 6g, and**
234 **Supplementary Fig. 7b**. The myeloid panel was used in **Fig. 4d and Supplementary Fig.**
235 **2b**. The cDC1 panel was used in **Supplementary Fig. 6b**. The lymphoid panel was used

in **Fig. 4d and Supplementary Fig. 2b**. The apoptosis panel was used in **Fig. S2e**. The cell cycle panel was used in **Fig. 2b and S2d**.

Related to Supplementary Fig. 1a

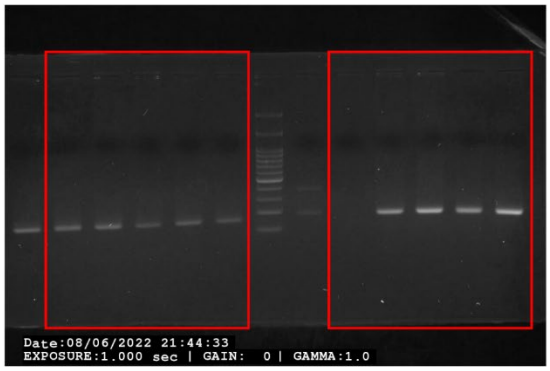

Supplementary Fig. 10. Uncropped scan of the electrophoresis gel image.

Uncropped scan of the electrophoresis gel image from Supplementary Fig. 1a.

Supplementary Reference

1 Ito, Y. *et al.* Comprehensive genetic profiling reveals frequent alterations of driver genes on the X chromosome in extranodal NK/T-cell lymphoma. *Cancer Res* (2024). https://doi.org/10.1158/0008-5472.Can-24-0132